Unveiling the High-Resolution Structure of Saturn's Rings from Cassini Radio Science Occultations

Student: Bryan Guo
Canyon Crest Academy, San Diego, CA, USA

Student: Brandon Xu
Philips Academy, Andover, MA, USA

Instructor: Ryan Maguire
Department of Mathematics, MIT
Cambridge, MA, USA

Instructor: Richard G. French
Department of Astronomy, Wellesley College
Wellesley, MA, USA

August 24, 2025

Declaration of Academic Integrity

The participating team declares that the paper submitted is comprised of original research and results obtained under the guidance of the instructor. To the team's best knowledge, the paper does not contain research results, published or not, from a person who is not a team member, except for the content listed in the references and the acknowledgment. If there is any misinformation, we are willing to take all the related responsibilities.

Names of team members: Bryan Guo, Brandon Xu

Signatures of team members

Name of the instructors: Richard G. French, Ryan Maguire

Signature of the instructor

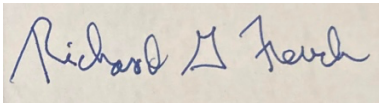

Date: 8/23/25

Unveiling the High-Resolution Structure of Saturn's Rings from Cassini Radio Science Occultations

Bryan Guo[1] and Brandon Xu[2]

[1] *Canyon Crest Academy, San Diego, CA*
[2] *Phillips Academy, Andover, MA*

ABSTRACT

Saturn's rings display a remarkable range of structures, from broad plateaus to fine spiral waves and ripples. Understanding the origins and dynamics of these features requires detailed profiling of the rings at the highest possible resolutions. Currently, the Cassini radio occultation profiles archived in the NASA Planetary Data System (PDS) have a radial resolution of 1 km. We introduce a novel diffraction inversion technique that achieves unprecedented radial resolutions down to 55 m, over an order of magnitude finer than existing profiles. In addition, two interpolation-based variants retain much of the accuracy of the primary approach and still significantly outperform the standard Fresnel quadratic approximation method at a fraction of the computational cost. The validity of high resolution reconstructions is assessed using a forward modeling test: starting from an ideal ring profile, we generate a synthetic signal under actual occultation geometry, process through our full reconstruction pipeline, and confirm that the expected profile is accurately recovered. Multi-resolution reconstructions are presented for five features of the C ring: the Maxwell ringlet, the Titan −1:0 nodal bending wave, two vertical bending waves, and short-wavelength ripples. For each feature, we compare profiles ranging from 1 km resolution, equivalent to those on the PDS, to 55 m, highlighting structures that emerge only at finer scales. Our advances open the possibility of studying previously inaccessible features in Saturn's rings and provide new opportunities for Kronoseismology, the study of Saturn's interior through its ring structure.

Keywords: occultations, planets: rings

Contents

1. INTRODUCTION

The rings of Saturn constitute a dense, self-gravitating disk of predominantly icy particles orbiting in Saturn's equatorial plane. These particles vary greatly in size, from micrometer-scale grains to boulders tens of meters across. Collectively, these particles exhibit dynamic features such as gaps, plateaus, self-gravity wakes, bending waves, and spiral density waves (Shu 1984). Understanding these features, especially at a fine scale, can provide valuable insights into the physics of self-gravitating particulate disks, moon-ring interactions, and even oscillations within the interior of Saturn itself (Marley & Porco 1993).

The Voyager missions in 1980 and 1981 delivered the first high-resolution (∼1 km) radio and stellar occultation profiles of the rings, enabling the first detection of small-scale features including sharp edges, narrow ringlets, satellite wakes, and a plethora of new wavelike phenomena (Shu 1984; Marouf et al. 1986). However, it was the Cassini-Huygens mission that ultimately revolutionized the study of Saturn's ring structure as it orbited Saturn between 2004 and 2017. The Imaging Science Subsystem (ISS) provided strikingly detailed images at radial resolutions of one to several kilometers, as illustrated in Figure 1 (Porco et al. 2005). Beyond imaging, occultation experiments have enabled even finer structural studies. Both the Ultraviolet Imaging Spectrograph (UVIS) and the Visible and Infrared Mapping Spectrometer (VIMS) on Cassini observed the light of background stars as they passed through the rings, providing one-dimensional "cuts" across the ring system. These stellar occultations provide a wide variety of observation geometries, with the ring opening angle varying from nearly face on to nearly edge on (Colwell et al. 2010; Nicholson et al. 2020).

In this paper, we focus on a third variety of occultations that make use of the radio signals transmitted by the Radio Science Subsystem (RSS) as Cassini passed through Saturn's rings. The probe conducted more than 100 radio occultation experiments, transmitting coherent phased radio signals of three different wavelengths through the rings to Earth-based radio telescopes in the NASA Deep Space Network (DSN). For each occultation profile, the intensity of the signal measured at Earth is affected by diffraction from the structure of the rings. Diffraction by ring material fundamentally limits the resolution of any occultation profile unless these effects are explicitly corrected. This limit,

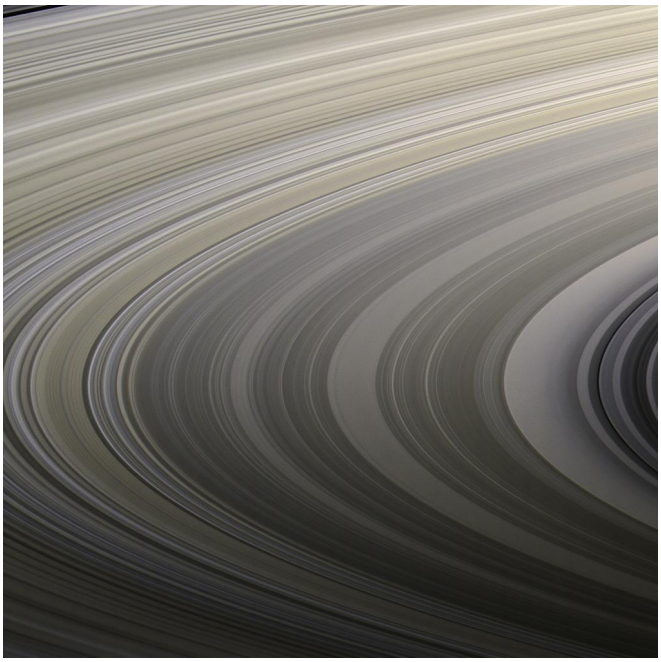

(a) A section of Saturn's B Ring showing a wide range of colors (NASA/JPL-Caltech 2018)

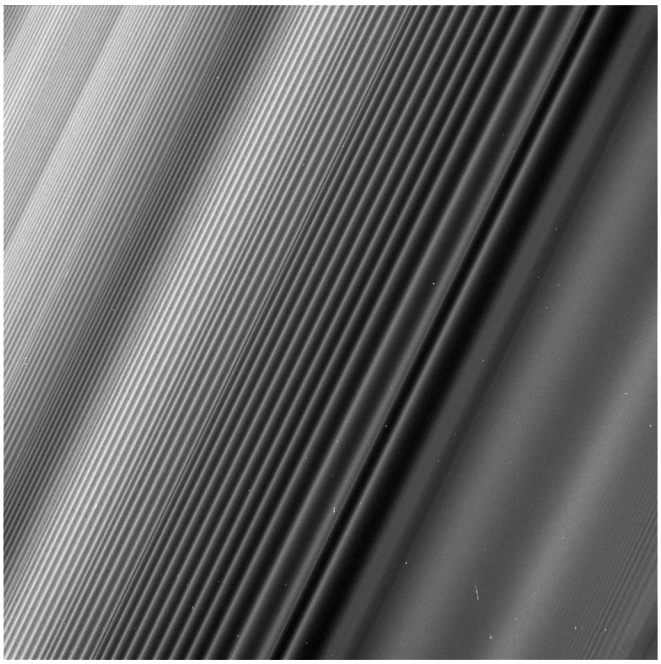

(b) A spiral density wave in the B ring (Janus 2:1) (NASA/JPL-Caltech 2017a)

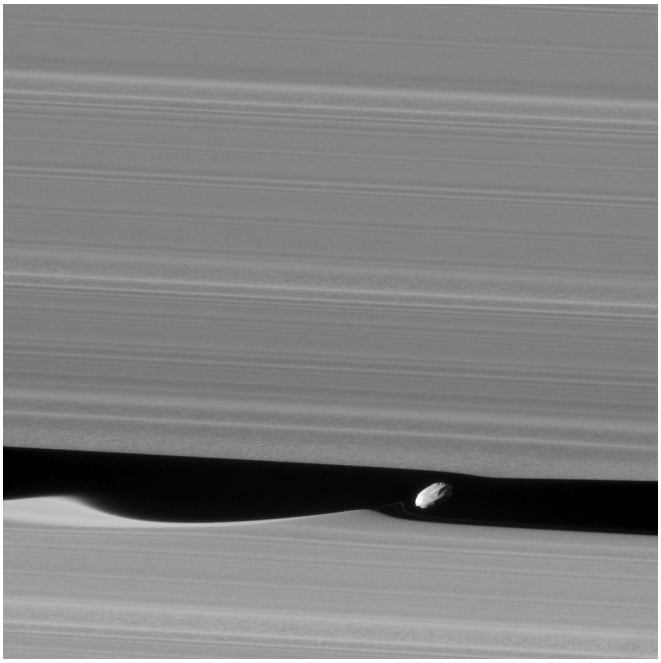

(c) Waves left in the wake of Saturn's moon Daphnis (NASA/JPL-Caltech 2017b)

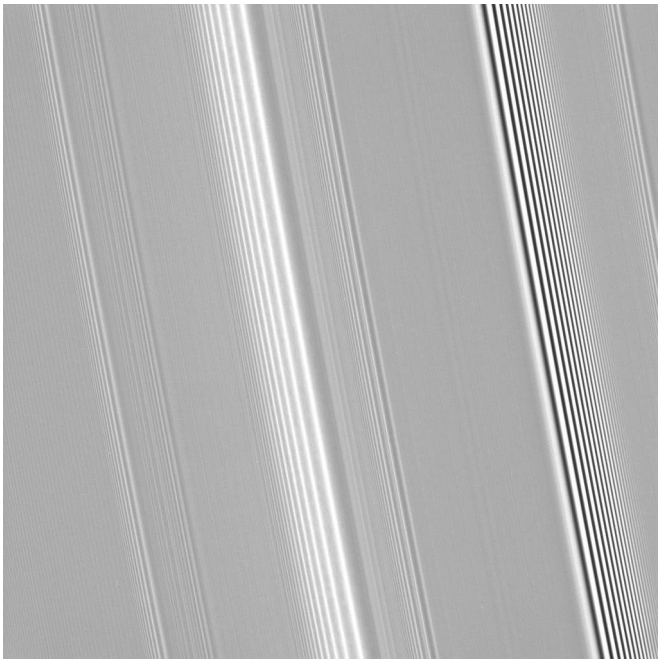

(d) A spiral density wave and bending wave, at center and right (NASA/JPL-Caltech 2008).

Figure 1. Images of fine-scale structure in Saturn's rings captured by the Imaging Science Subsystem.

set by the Fresnel scale $F \sim \sqrt{\frac{\lambda D}{2}}$, where λ is the wavelength and D is the distance from the spacecraft to the ring plane intersection, can reach 10 km or more for certain Cassini geometries. Fortunately, since the RSS, like Voyager 1, records the full complex signal including phase, it is possible to invert the diffraction integral to reconstruct a profile at a resolution much finer than F (Marouf et al. 1986). The ability to resolve fine-scale structures in the rings,

demonstrated by both Voyager and Cassini, has led to the development of *Kronoseismology*, which uses wave patterns in Saturn's rings to study the planet's interior (Marley & Porco 1993; Hedman & Nicholson 2013).

The remainder of this paper is organized as follows. In Section 2 we discuss the scientific motivation behind the importance of obtaining high-resolution reconstructions of various ring structures. In Section 3.1, we review the mathematics of diffraction reconstructions from radio occultations and review key definitions of Cassini RSS occultation geometry. Section 4 introduces our primary inversion technique alongside two efficient interpolation-based variants, and compares their accuracy and computational cost with the standard method based on Fresnel quadratic approximation. In Section 5 we introduce a forward modeling framework to validate our new method at the highest resolutions, and under the most extreme geometric configurations. In Section 6 we apply our new reconstruction method to several features in the C ring, comparing results over a range of resolutions and retrieving opacity profiles of waves at resolutions as fine as 55 m, providing qualitative assessments of the benefits of increased resolution. In Section 7, we discuss the scientific value of our study within the field of Kronoseismology, as well as potential future directions for exploration with these new reconstruction techniques. Appendix A contains details of the derivations of the coefficients used in the octic and hexadecic inversion techniques introduced in Section 4, and Appendix B contains a derivation of collapsing the double integral for $\hat{T}$ into a single integral via stationary phase approximation to the ϕ-integral in the forward model. Collectively, these analyses establish the conditions under which high-resolution opacity profiles can be robustly obtained, and provide a foundation for future Kronoseismological investigations.

2. SCIENTIFIC MOTIVATION

Kronoseismology is the ring-based analogue of helioseismology: resonances between Saturn's internal normal-mode oscillations and orbiting ring particles launch waves whose pattern speeds encode the frequencies of the driving modes. These waves fall into two main categories. Spiral density waves are driven at inner or outer Lindblad resonances (ILRs/OLRs), where Saturn's oscillations compress and rarefy material within the ring plane. Bending waves arise at vertical resonances (IVRs/OVRs), which tilt the local ring plane and create vertical corrugations. Because each mode's frequencies are dependent on the planet's internal density, composition, and rotation, the rings effectively act as a seismometer that probes the planet's interior. Unlike traditional gravity or magnetic field measurements, Kronoseismology is sensitive to the planet's density stratification and differential rotation, proving to be the most sensitive method to detect planetary acoustic oscillations (Marley & Porco 1993).

Marley and Porco first predicted that Saturn's fundamental modes ("f-modes") would drive outward-propagating waves at their outer Lindblad resonances in the C ring. Two decades later, Hedman & Nicholson (2013) used stellar occultations from Cassini's VIMS instrument to identify six unexplained, multi-armed density waves whose pattern speeds matched those predicted f-mode frequencies to within ∼0.1%—the first direct detection of planetary oscillations via the rings. Subsequent papers in the Kronoseismology series (I-VII) have expanded the census to $\gtrsim$ 40 waves, including higher-order g-modes and possible inertial-gravity hybrids, and have mapped them throughout the inner and middle C ring as well as narrow parts of the B ring (Hedman & Nicholson 2013; Hedman and Nicholson 2014; French et al. 2019; Hedman et al. 2019; French et al. 2021; Hedman et al. 2022; Afigbo et al. 2025).

Certain features have even been traced back to discrete external events. For example, a system of small periodic ripples in the inner C ring, most prominent between 74500 km and 77765 km, has been attributed most likely to the aftermath of an impact with a debris cloud in late 1983 (French et al. 2025; Hedman et al. 2007, 2011). These vertical corrugations, exhibiting wavelengths as short as $\sim$ 1 km and evolving over time, encode information about the ring's dynamical response, viscosity, and collisional properties. More recently, higher-resolution RSS data have provided further evidence for the impact results (French et al. 2025).

However, fully resolving the structure and evolution of these subtle features is fundamentally limited by the resolution of available data. Currently, the best opacity profiles constructed from Cassini RSS data, which are archived in the NASA Planetary Data System (PDS), are limited to resolutions of 1 km. Higher resolution reconstructions would enable the detection of additional mode-driven waves and yield more precise constraints on the morphology and propagation of previously identified features. Indeed, many predicted resonances with higher-degree gravity and internal modes

should lie at radii where the corresponding wavelengths are at hundreds of meters (French et al. 2021; Hedman et al. 2022). Mapping and characterizing these subtle waves may help determine the depth of Saturn's stratified layer (Mankovich & Fuller 2021), as well as constrain the internal profile of the C ring itself. Meeting these scientific objectives requires reconstructing radio occultation profiles at resolutions closer to or surpassing 100 m, an entire order of magnitude improvement over archived Cassini products.

Although Marouf et al. (1986) first demonstrated a practical inversion of the Fresnel diffraction integral, producing Voyager-based opacity profiles at 900 m resolution, the computational techniques and geometric assumptions underlying such inversions remain a limiting factor when applied to resolutions on the hundred-meter scale. In particular, the reconstruction depends on analytic approximations, such as low-order polynomial interpolations, whose domains of validity are insufficient at higher resolutions. Consequently, it is necessary to refine these inversion methods, which involves improving their accuracy in modeling diffraction in extreme geometric configurations, as well as managing the effects of noise. Inherently, there is also a tradeoff in computational cost when attempting to construct higher resolution profiles which must be balanced as well.

A detailed, high-resolution characterization of both spiral density and bending waves is crucial to revealing the small-scale physics that govern how energy, angular momentum, and mass are distributed in particles. Such reconstructions will reveal the fine-scale radial and vertical structure of spiral density and bending waves, enabling precise measurements of their amplitudes and wavelengths. In particular, high-resolution, high signal-to-noise radio reconstructions could be used to measure the vertical extent of bending waves, a property inaccessible to VIMS, UVIS, or previous RSS datasets. By combining analyses of a bending wave across multiple observations, it becomes possible to reconstruct a three-dimensional model of the spiral wave Furthermore, sub-kilometer resolutions in optical depth profiles reveal the onset of gravitational instabilities and behavior between colliding particles—processes that remain hidden at kilometer-scale resolution. When combined with stellar occultation analyses from Cassini's VIMS and UVIS, which have provided the bulk of detailed ring wave detections to date (Colwell et al. 2009; Hedman & Nicholson 2013; PDS Rings Node 2025), these radio science profiles will yield a synergistic view of ring response to Saturn's oscillations and constrain the underlying properties and particle size distributions that govern wave propagation. By reconstructing opacity profiles at sub-100 m resolutions, we gain sharper constraints on Saturn's internal oscillations and a more complete understanding of the structure of the waves themselves.

3. BACKGROUND

3.1. *Diffraction*

Details of the Saturnocentric occultation geometry have been discussed at length elsewhere (Marouf et al. (1986), Marouf et al. (1982)). Hereafter we adopt the naming conventions of the occultation geometry as presented in Marouf et al. (1986). The reconstruction of the ring transmittance relies on a Huygens-Fresnel description of coherent diffraction through an infinitesimally thin planar "gray screen" (Born and Wolf (2019), Marouf et al. (1986), Marouf et al. (1982)). Consider a monochromatic plane wave of unit amplitude and wavenumber $k = \frac{2\pi}{\lambda}$ incident along $\hat{\mathbf{u}}$ upon a thin, circularly symmetric screen located in the xy-plane. For a distant observer at $\mathbf{R}$, the complex field E_c is given by the superposition of secondary spherical wavelets emitted from each infinitesimal area element $d\boldsymbol{\rho}$ on the screen:

$$E_c \approx E_0 \iint_S \left[\frac{\mu_0}{i\lambda} T(\boldsymbol{\rho}) \exp(ik\hat{\mathbf{u}} \cdot \boldsymbol{\rho})\right] \frac{\exp(ik\|\mathbf{R} - \boldsymbol{\rho}\|)}{\|\mathbf{R} - \boldsymbol{\rho}\|} d\boldsymbol{\rho}, \tag{1}$$

where E_0 is a constant reference amplitude, $\mu_0 = \sin B$ is the obliquity factor, and $T(\boldsymbol{\rho})$ is the complex transmittance encoding both amplitude attenuation and phase delay imparted by the ring material. To remove geometric phase terms introduced by the spacecraft–observer path, one defines the normalized coherent field

$$\hat{T}(\boldsymbol{\rho}_0) = \frac{E_c}{E_0} \exp(-ik\hat{\mathbf{u}} \cdot \mathbf{R}), \tag{2}$$

which satisfies $|\hat{T}| = 1$ in the absence of ring effects. In the occultation geometry of Marouf et al. (1986), we obtain the following crucial integral relationship between T and $\hat{T}$:

$$\hat{T}(\rho_0) = \frac{\mu_0}{i\lambda} \int_0^\infty \rho T(\rho) d\rho \int_0^{2\pi} \frac{\exp\left(i\psi(\rho_0, \phi_0; \rho, \phi)\right)}{\|\mathbf{R} - \boldsymbol{\rho}\|} d\phi. \tag{3}$$

Exploiting the near-circular symmetry of the rings permits reduction of the two–dimensional transform in Equation (3) to a one-dimensional radial integral, making it possible to invert the observed $\hat{T}(\rho_0)$ along a single occultation track and thereby recover the radial profile of $T(\rho)$. In particular, applying the stationary phase approximation to ψ, the Fresnel phase, by finding the stationary azimuth angle in the ϕ integral about some critical point $\phi = \phi_s$ gives

$$\hat{T}(\rho_0) = \frac{1-i}{2F} \int_{-\infty}^{\infty} T(\rho) \exp(i\psi(\rho_0, \phi_0; \rho, \phi_s)) d\rho, \tag{4}$$

where

$$F = \sqrt{\frac{\lambda D}{2} \frac{1 - \cos^2 B \sin^2 \phi_0}{\sin^2 B}} \tag{5}$$

is the Fresnel scale (Marouf et al. 1986). To recover an approximate inverse transform, we replace the plane of integration from the (ρ, ϕ) plane to the (ρ_0, ϕ_0) plane, and take the complex conjugate of the Fresnel kernel. Consequently, the forward-kernel factor

$$\frac{1-i}{2F} \exp(i\psi(\rho_0, \phi_0; \rho, \phi_s)) \tag{6}$$

is replaced by its conjugate,

$$\frac{1+i}{2F} \exp(-i\psi(\rho_0, \phi_0; \rho, \phi_s)), \tag{7}$$

thereby defining the desired approximate inverse operation.

The accuracy of the diffraction-limited reconstructed profile is highly dependent on the Fresnel phase ψ. Explicitly, following Marouf et al. (1986), ψ is given by

$$\psi(\rho_0, \phi_0; \rho, \phi) = kD[\sqrt{1 + 2\xi + \eta} - (1 + \xi)], \tag{8}$$

where

$$\xi = \frac{\cos B(\rho_0 \cos\phi_0 - \rho \cos\phi)}{D}, \tag{9}$$

$$\eta = \frac{\rho_0^2 + \rho^2 - 2\rho\rho_0 \cos(\phi - \phi_0)}{D^2}, \tag{10}$$

and

$$D = \|\mathbf{R} - \boldsymbol{\rho}_0\|. \tag{11}$$

Since ψ is proportional to the wavenumber k, which in practice is very large, even slight deviations in ξ and η that characterize the transverse and longitudinal offsets between source and receiver can produce significant differences in the phase term.

3.2. *Practical Considerations for Reconstruction*

Having established the theoretical basis for reconstructing ring transmittance, we now address several practical factors that influence the accuracy and utility of such reconstructions. We first review several key concepts and terms relevant to radio occultation analyses with Cassini RSS. The *normal optical depth* quantifies the attenuation of incident radiation by ring material when viewed in the normal direction to the ring plane and serves as a direct measure of particle column density. Cassini radio observations were conducted in three wavelength bands—Ka ($\lambda \sim 0.9$ cm), X ($\lambda \sim 3.6$ cm), and S ($\lambda \sim 13$ cm)—each of which probes different particle-size regimes. Occultation tracks are classified as *ingress-egress*, in which the spacecraft's line of sight cuts straight across the rings in the east-west direction

as viewed on the sky from Earth, so that the track is approximately in the radial direction, from *chord* occultations, which transect the rings as viewed from the Earth, more vertically in the north-south direction. Throughout this study, we refer to individual observations by their Cassini revolution ("Rev") number, wavelength band designation (Ka or X), and DSN number, which denotes the specific Earth-based radio telescope that received the signal.

The applicability of the reconstruction methods depends strongly on the width of the processing window W, since the Fresnel phase ψ continually varies over the radial range. Specifically, smaller values of W make lower-order approximations of ψ more feasible. The particular value of W is derived from F and the processing resolution, ΔR_w, given by Eq. (11) in Marouf et al. (1986). In addition, at low-numbered Revs, the magnitude of the ring opening angle B was close to its maximum of $\sim 26.7°$, equal to the relative tilt of Saturn's rotational axis to the ecliptic plane. As the Rev numbers increase, $|B|$ decreases, causing F to increase dramatically in turn (PDS Rings Node 2025). The result is that later occultations are much less forgiving to approximation errors in ψ. The signal's wavelength also plays a significant role in determining the window size W. For identical geometry and processing resolution, W scales linearly with the radio wavelength λ; thus, the window size for the Ka band is approximately a quarter of that for the X band in the same observation.

Larger window widths will inevitably lengthen both forward modeling and inversion time. In using the standard forward model in radio occultation reconstructions as the Fresnel transform, evaluating the convolution with standard Fourier transform techniques is $O(N \log N)$, where $N \approx W/\Delta R_w$ is the number of samples of a window of width W sampled at a resolution of ΔR_w. Practically, doubling W approximately doubles the run time for a fixed ΔR_w.

The occultation geometry also governs the conditions under which each type of wave can be most effectively detected. Density waves benefit from larger $|B|$ as the signal-to-noise per radial sample is typically higher, so radial compressions and rarefactions are sampled more cleanly. On the other hand, bending and vertical waves produce out-of-plane displacements and tilts of the local ring plane. Those vertical corrugations modulate the slant column density and phase most strongly when the line of sight skims the plane, that is, at smaller $|B|$. The azimuth angle ϕ also plays a key role. Depending on whether the line of sight crosses the corrugations perpendicular or parallel to their crests, the modulation strength can vary greatly. This combined dependence is captured by the effective ring opening angle, $B_{\rm eff}$, given by

$$\tan B_{\rm eff} = \frac{\tan B}{\cos \phi}. \tag{12}$$

When ϕ is close to $0°$ or $180°$, the line of sight is perpendicular to the wave crests, making vertical displacements easier to detect. In practical terms, density waves are best observed at high $|B|$, corresponding to the early Cassini revolutions when the rings were more open, while bending waves are most clearly observed at low $|B|$ during later Revs, especially when $|B_{\rm eff}|$ is minimized.

4. OBSERVATIONS AND METHODS

In this section, we evaluate four distinct methods used in the diffraction-based reconstruction of Saturn's ring optical depth profiles from Cassini RSS occultation data. Each method is characterized by the level of approximation used in representing the Fresnel phase $\psi(\rho_0, \phi_0; \rho, \phi_s)$. Specifically, we compare the existing approach using the traditional Fresnel quadratic approximation with three new techniques we have developed: a full Newton–Raphson scheme enhanced with a modification to the Filon quadrature method and two higher-order Lagrange interpolation variants. For each approach, we outline the underlying mathematical basis and assess its computational efficiency. We also introduce the observational dataset used in this study, followed by direct comparisons of reconstructed profiles that highlight how these approaches differ in recovering fine-scale ring structure.

4.1. *Approximation via the Fresnel Quadratic*

As described by Marouf et al. (1986), the *Fresnel* reconstruction method provides a simple approach to approximate the Fresnel phase to be used in the diffraction reconstruction integral for $\hat{T}(\rho_0)$ using a quadratic approximation. In

this method, the stationary azimuthal angle ϕ_s is estimated using a tangent line approximation equivalent to a single iteration of the Newton-Raphson method using ϕ_0 as the initial estimate. Then, ψ is expanded about this first-order estimate $\phi_{s,1}$, retaining only up to the quadratic term. As a result, we obtain the following quadratic approximation for the phase:

$$\psi(\rho_0, \phi_0; \rho, \phi_{s,1}) \approx \frac{\pi}{2}\left(\frac{\rho - \rho_0}{F}\right)^2, \tag{13}$$

where F is the Fresnel scale (Marouf et al. 1986).

Due to its simplicity, this method is the least computationally intensive of those we investigate, as reflected in the comparison of execution times found in Table 2. However, this simplicity comes at the cost of accuracy in certain situations. For instance, when the opening angle of the ring B decreases in the later Revs, the Fresnel scale increases greatly, causing the width of the required window of integration, W, to become extremely large. A similar effect is observed as the processing resolution of the reconstruction becomes finer. At such large processing windows, sometimes spanning thousands of kilometers, a quadratic approximation is insufficient to accurately reconstruct ring profiles.

4.2. *Approximation via Newton-Raphson*

Our novel *Newton* reconstruction method provides a refined alternative to the Fresnel quadratic approximation by evaluating the Fresnel phase $\psi(\rho_0, \phi_0; \rho, \phi_s)$ exactly rather than through low-order expansions. The stationary azimuthal angle ϕ_s is determined through multiple iterations of the Newton–Raphson method, yielding a converged solution rather than a first-order estimate. Moreover, prior reconstruction methods, most notably the Fresnel method, adopt the following simple estimate for ψ'' given by

$$\psi_s'' \approx kD(1 - \cos^2 B \sin^2 \phi_0)\left(\frac{\rho_0}{D}\right)^2, \tag{14}$$

as shown in equation (A3-c) of Marouf et al. (1986). However, at later Revs and higher resolutions, such an estimation yields spurious transmittance profiles, undermining the accuracy of the reconstructed radial structure. Instead of using such approximations for ψ'', the Newton reconstruction method computes the exact value of ψ''.

To do so, instead of assuming a constant value of $D = \|\mathbf{R} - \boldsymbol{\rho}\|$, we now let (x, y, z) be independent variables corresponding to the Cassini's location relative to the center of Saturn and $\boldsymbol{\rho} = (\rho\cos\phi, \rho\sin\phi)$ the coordinates of the $\boldsymbol{\rho}$ vector. Then, we write

$$\|\mathbf{R} - \boldsymbol{\rho}\| = \sqrt{(x - \rho\cos\phi)^2 + (y - \rho\sin\phi)^2 + z^2}, \tag{15}$$

and compute ψ'' with the multivariable chain rule, where ψ is given explicitly as:

$$\psi = k\left[\|\mathbf{R} - \boldsymbol{\rho}\| - \frac{\mathbf{R} - \boldsymbol{\rho}_0}{\|\mathbf{R} - \boldsymbol{\rho}_0\|} \cdot (\mathbf{R} - \boldsymbol{\rho})\right]. \tag{16}$$

This approach ensures that the Fresnel phase fully accounts for the true spacecraft-ring geometry at each sampling point across the processing window, yielding fine-scale reconstructions that, in the absence of noise and under the assumption that the ring structure is well approximated as one-dimensional, can robustly recover ring features even in the most extreme occultation geometries. While this method's reliance on the exact evaluation of ψ'' and full incorporation of the instantaneous spacecraft-ring geometry incur a significant increase in computation time, the resulting reconstructions exhibit dramatically reduced errors which thereby enable quantitative analyses of fine-scale radial structures unattainable with traditional low-order approximations.

Finally, we note that the actual inversion calculation requires evaluating a highly oscillatory integral, for which we apply an adapted version of Filon's quadrature method. The details and justification of this approach is discussed in more detail in Section 5.

4.3. *Approximation via Octic and Hexadecic Interpolation*

In Marouf et al. (1986) a fourth-order polynomial approximation for ψ is obtained by fitting computed values of ψ over the window width W. This allows for $T(\rho)$ to retain its convolution properties and result in efficient reconstruction

using fast Fourier transform techniques. At resolutions approaching 200 m, however, a polynomial of fourth-order ceases to adequately capture the true transmittance profile of the ring. To account for the inadequacy of a uniform fourth-order fit at these resolutions, we introduce a more accurate kernel representation by fitting ψ over a greater number of points across the window. In this method, the stationary azimuthal angle is found in the same way as in our Newton reconstruction method. In particular, we develop eighth and sixteenth-order approximations for ψ by using the Lagrange interpolating polynomials

$$\psi = \sum_{n=1}^{8} C_n(\rho - \rho_0)^n \qquad \text{and} \qquad \psi = \sum_{n=1}^{16} C_n(\rho - \rho_0)^n.$$

It is important to emphasize that coefficients C_n are not fixed constants as in a conventional interpolating polynomial, but rather depend on the changing geometric parameters ϕ_s, ϕ_0, ρ_0, B, and D. The derivation of the coefficients C_n can be found in Appendix A.

4.4. *Summary of Observational Dataset*

The table below lists each ring feature selected for high-resolution reconstruction in this study, along with the specific Cassini RSS observations used to examine each target. Each RSS observation is labeled by a three-digit revolution number, occultation direction (I for ingress or E for egress), wavelength band (S, X, or Ka), and DSN number. The letter "W" found at the beginning of some feature names, such as "W74.93" and "W74.94", specifically refers to a wave feature, and the number following indicates the radial location in thousands of kilometers.

Observation	Feature Name	Feature Type	Radial Range (km)	B	B_{eff}
Rev007E X43	Maxwell Ringlet	OLR / Ringlet	87480–87560	$-23.57°$	$53.16°$
Rev125I X34	Titan −1:0	IVR	77530–77610	$4.77°$	$15.61°$
Rev125I X34	Titan −1:0 (inner)	IVR	77530–77565	$4.77°$	$15.61°$
Rev125I X34	W74.93, W74.94	OVR	74930–74950	$4.77°$	$15.70°$
Rev133I X25	C ring ripples	—	77700–77750	$1.88°$	$9.21°$
Rev133E X43	W80.98	OLR	80960–81000	$1.88°$	$-12.30°$

Table 1. Summary of Cassini RSS occultations and ring features examined in this study. For each observation, the revolution, direction, and band are given, along with the feature name, type, analyzed radial range, ring opening angle B, and effective opening angle B_{eff}.

4.5. *Comparison of Reconstruction Methods*

In order to evaluate the accuracy of the reconstruction methods, we present normal optical depth profiles for the spiral density wave W80.98 (Colwell et al. 2009; Hedman & Nicholson 2013) using data from the Rev133E X43 observation. This particular observation is notable for its exceptionally small ring opening angle, which imposes a stringent test on the accuracy of each method's phase approximation due to the large Fresnel scale $F \approx 10$ km as a result. For each method, we plot reconstructions spanning resolutions from 1 km, equivalent to the available PDS archive results, down to 100 m, representing an order-of-magnitude improvement. Within these plots, "Newton8" refers to the octic interpolation method, and "Newton16" refers to the hexadecic interpolation method. Each plot contains a four-panel comparison of the normal optical depth profile as a function of radial position for W80.98, with the Fresnel reconstruction shown in the top left, octic reconstruction in the top right, hexadecic reconstruction in the bottom left, and the Newton reconstruction in the bottom right. Throughout this section, we use the Newton reconstruction as the reference for relative comparison, as it involves the fewest mathematical simplifications in the process. The direct validation of the Newton method's absolute accuracy for this observation at 100 m resolution will be presented in the following section.

We begin by comparing reconstructions of W80.98 at resolutions of 1000 m, 500 m, 300 m, and 200 m, shown in Figure 2.

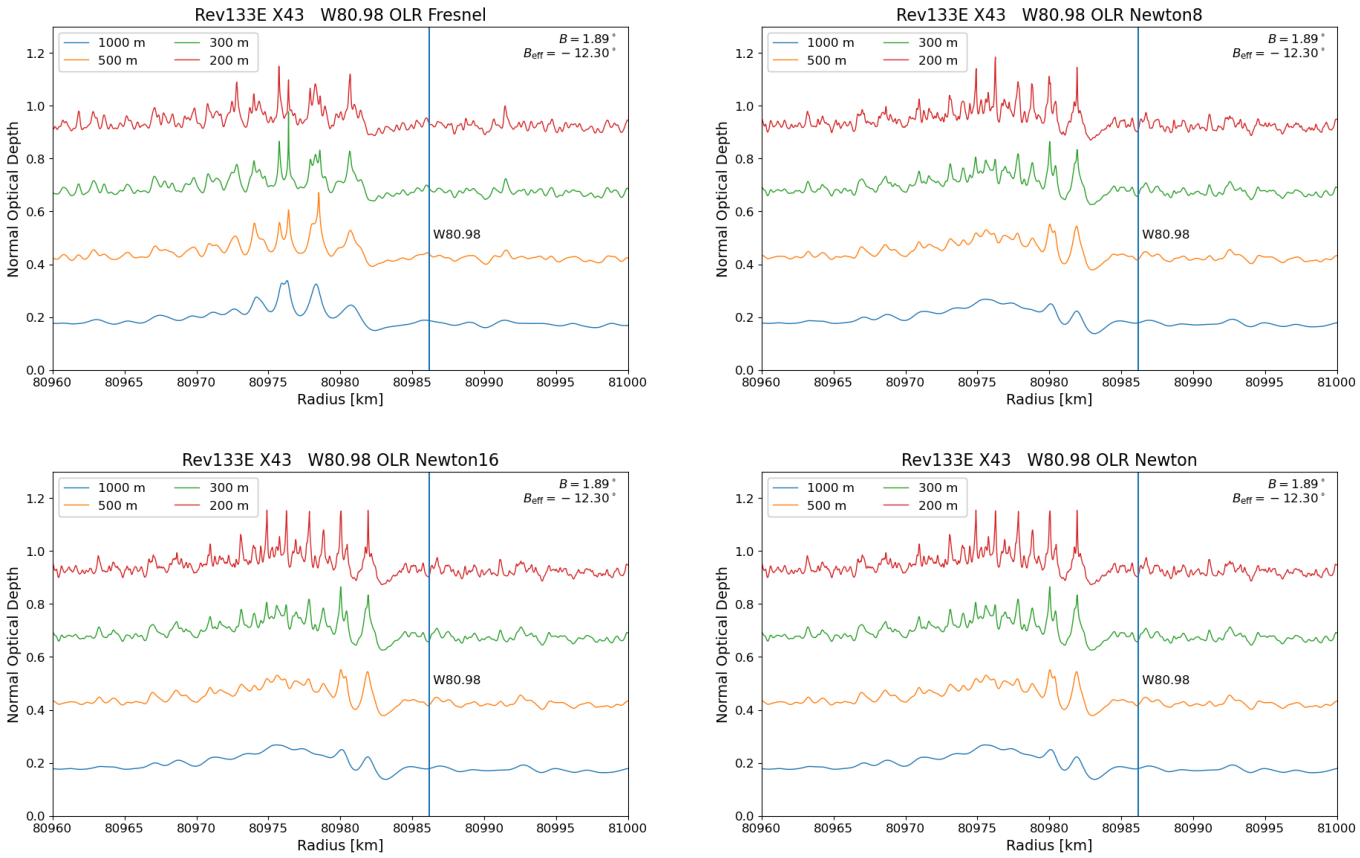

Figure 2. Comparison of four reconstruction methods applied to W80.98 for resolutions between 1 km and 200 m (Rev133E X43)

The key result is that the Fresnel quadratic approximation produces profiles that are visibly inaccurate even at 1 km resolution; the reconstructed structure deviates significantly from those obtained with our new methods across all spatial scales. Meanwhile, the octic reconstruction is identical to the Newton-based reconstruction down to 300 m. Minor differences, such as subtle discrepancies in peak heights around 80975–80977 km, only begin to appear in the octic profile at 200 m resolution. However, the overall structure remains well preserved, with a root mean square deviation (RMSD) in τ of approximately 0.005. Notably, the hexadecic and Newton reconstructions remain indistinguishable even at 200 m, providing strong evidence for the reliability of these higher-order methods at this resolution.

Given the near-indistinguishability of the three Newton-based methods at coarser resolutions, we also present reconstructions of W80.98 from 300 m down to 100 m (Figure 3). The full Newton reconstruction maintains a cleanly structured, well-defined profile across all examined radial resolutions. In contrast, both the octic and hexadecic interpolations produce reconstructions with a pronounced stability breakdown at 100 m resolution: their profiles become overwhelmingly noisy and frequently dip below zero optical depth, rendering them unusable. Nonetheless, the octic interpolation remains reliable down to resolutions of 150 m, as any deviations compared to the Newton reconstruction remain small (τ RMSD ≈ 0.01). However, at 125 m, accuracy degrades significantly, with very little structure being accurately retained. The hexadecic interpolation improves the achievable resolution limit as it maintains close agreement with the Newton solution down to 125 m (τ RMSD ≈ 0.00557).

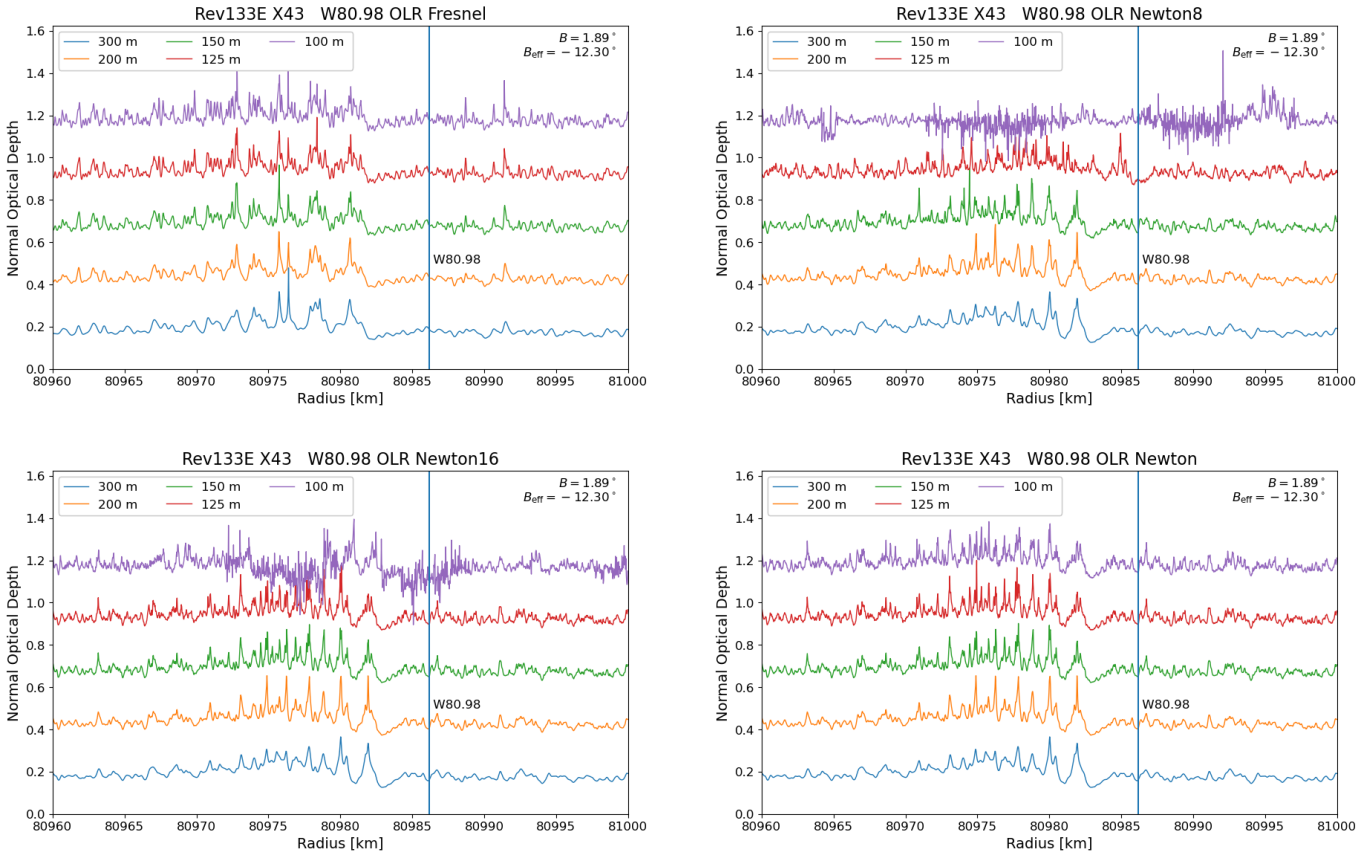

Figure 3. Comparison of four reconstruction methods applied to W80.98 for resolutions between 300 m and 100 m (Rev133E X43)

While we have shown that the full Newton-based reconstruction method is required for the most extreme occultation geometries or the highest resolutions, it is considerably more computationally intensive than other approaches. Table 2 summarizes these computational tradeoffs for processing the Huygens gap, spanning approximately 400 km, on the same Rev133E X43 observation. For general use cases with moderate opening angles, resolutions above 125–150 m, or wide radial ranges, the octic and hexadecic interpolation methods offer a compelling alternative: they deliver reconstructions that are dramatically more accurate than the Fresnel quadratic approximation, with only a two- to three-fold increase in processing time relative to Fresnel. In comparison, the full Newton method is 20–30 times slower than Fresnel.

Reconstruction Method	Processing time (seconds)
Fresnel	16
Octic Interpolation	36
Hexadecic Interpolation	41
Newton	419

Table 2. Execution time for processing the Huygens gap at 125 m resolution (Rev 133E, X43) using various reconstruction methods. Benchmarks were performed on a machine with 64 GB RAM, AMD Ryzen 9 3900X CPU, running on Debian GNU/Linux 12.

5. FORWARD MODEL VALIDATION

While the preceding analysis in Section 4.5 treated the Newton reconstruction method as the reference for benchmarking other approaches, its absolute accuracy has not yet been rigorously established. To address this, we now undertake a direct validation of the Newton-based reconstructions by applying a forward model.

The Fresnel forward and inverse transforms given in Marouf et al. (1986) rely on several approximations, many of which decrease the validity of reconstruction and accuracy verification. Here, we provide a new and improved forward model using fewer approximations on the Fresnel phase, but still retaining the convolution property of the integral, in order to ensure the possibility of an analytical inverse. We then use this forward and inverse model on a perfect left straightedge at 100 m resolution with real occultation geometry to validate the accuracy of our reconstructions.

Unlike the ideal geometry assumed in Marouf et al. (1986), where $\hat{\mathbf{u}} \cdot \hat{\mathbf{y}} = 0$, we instead compute the full Fresnel kernel. Here,

$$\hat{\mathbf{u}} = \frac{\mathbf{R} - \boldsymbol{\rho}_0}{\|\mathbf{R} - \boldsymbol{\rho}_0\|} \tag{17}$$

represents the normalized relative position vector of $\mathbf{R}$ with respect to $\boldsymbol{\rho}_0$. To retain accuracy, we keep $\boldsymbol{\rho}, \boldsymbol{\rho}_0$, and $\mathbf{R}$ as vectors in Cartesian form.

As in Section 3.1, we model the diffraction pattern seen by a radio wave passing through a thin screen using the Rayleigh-Sommerfeld equation, obtained from the wave equation. Adopting notation from Section 3.1, writing out Eq. (2) in its entirety gives the following for $\hat{T}$:

$$\hat{T}(\boldsymbol{\rho}_0) = \frac{\mu_0}{i\lambda} \iint_S T(\boldsymbol{\rho}) \frac{\exp\left(ik(\hat{\mathbf{u}} \cdot (\boldsymbol{\rho} - \mathbf{R}) + \|\boldsymbol{\rho} - \mathbf{R}\|)\right)}{\|\mathbf{R} - \boldsymbol{\rho}\|} d\boldsymbol{\rho}, \tag{18}$$

where $\boldsymbol{\rho}$ is the integration variable, and $\boldsymbol{\rho}_0$ denotes the point at which the observer–source line of sight intersects the screen S. Substituting Eq. (16) into Eq. (18) yields the forward model

$$\hat{T}(\boldsymbol{\rho}_0) = \frac{\mu_0}{i\lambda} \iint_S T(\boldsymbol{\rho}) \frac{\exp(i\psi(\boldsymbol{\rho}, \boldsymbol{\rho}_0, \mathbf{R}))}{\|\mathbf{R} - \boldsymbol{\rho}\|} d\boldsymbol{\rho}. \tag{19}$$

Assuming radial symmetry of the transmittance, $T(\boldsymbol{\rho}) = T(\rho)$, and working in polar coordinates with $\boldsymbol{\rho} = (\rho, \phi)$ and $\boldsymbol{\rho}_0 = (\rho_0, \phi_0)$, the integral reduces to

$$\hat{T}(\rho_0) = \frac{\mu_0}{i\lambda} \int_0^\infty \rho T(\rho) \int_0^{2\pi} \frac{\exp(i\psi(\boldsymbol{\rho}, \boldsymbol{\rho}_0, \mathbf{R}))}{\|\mathbf{R} - \boldsymbol{\rho}\|} d\phi d\rho. \tag{20}$$

Applying the stationary phase approximation to the ϕ-integral collapses the double integral to a single integral without compromising the accuracy of the model:

$$\hat{T}(\rho_0) \approx \frac{1 - i}{2F} \int_0^\infty T(\rho) \exp(i\psi(\boldsymbol{\rho}_s, \boldsymbol{\rho}_0, \mathbf{R})) d\rho, \tag{21}$$

where $\boldsymbol{\rho}_s = (\rho, \phi_s)$ with ϕ_s the stationary azimuth angle. A more detailed derivation for the simplification of the double integral can be found in Appendix B. Under the classical Fresnel approximation for $\psi(\boldsymbol{\rho}_s, \boldsymbol{\rho}_0, \mathbf{R})$, one obtains an explicit inverse. By analogy, we obtain the following approximate inverse for Eq. (21):

$$T(\rho) \approx \frac{1 + i}{2F} \int_0^\infty \hat{T}(\rho_s) \exp(-i\psi(\boldsymbol{\rho}_s, \boldsymbol{\rho}_0, \mathbf{R})) d\rho_0. \tag{22}$$

In the forward model, $\mathbf{R}$ and $\boldsymbol{\rho}_0$ are held fixed while $\boldsymbol{\rho}$ varies. In practice, the observer may also move; because $\boldsymbol{\rho}_0$ depends on both the position vector $\mathbf{R}$ and the incidence direction of the incoming wave, the inverse formulation must allow $\mathbf{R}$ to vary along with $\boldsymbol{\rho}_0$. Together, Eqs. (21) and (22) provide forward and inverse models which are robust at the highest resolutions.

For some high resolution reconstructions, the Fresnel phase ψ grows rapidly at the edge of the window of integration. This causes $\exp(i\psi(\boldsymbol{\rho}_s, \boldsymbol{\rho}_0, \mathbf{R}))$ to be highly oscillatory. Unlike the azimuthal component, which was handled using the stationary phase approximation, this integral over the radius has a small scale factor, roughly $\pi/2F^2$. Stationary phase does not apply, and the simpler numerical integration techniques (Riemann sums, Simpson's method, etc.) are poorly suited for highly oscillatory integrals. To mitigate this, we have developed a modification of the Filon quadrature method, applied to handle ψ in piece-wise linear sections. This new quadrature method is exact when the diffracted data $\hat{T}$ is piece-wise linear, and produces an accurate numerical integral for real data as well (i.e., the observed $\hat{T}$ values).

Figure 4 depicts a plot of the forward and inverse model applied to an ideal left straightedge set to 1 to the left of 87500 km and 0 to the right of 87500 km. The plot corresponds to a 100 m resolution reconstruction for the Rev133E X43 occultation.

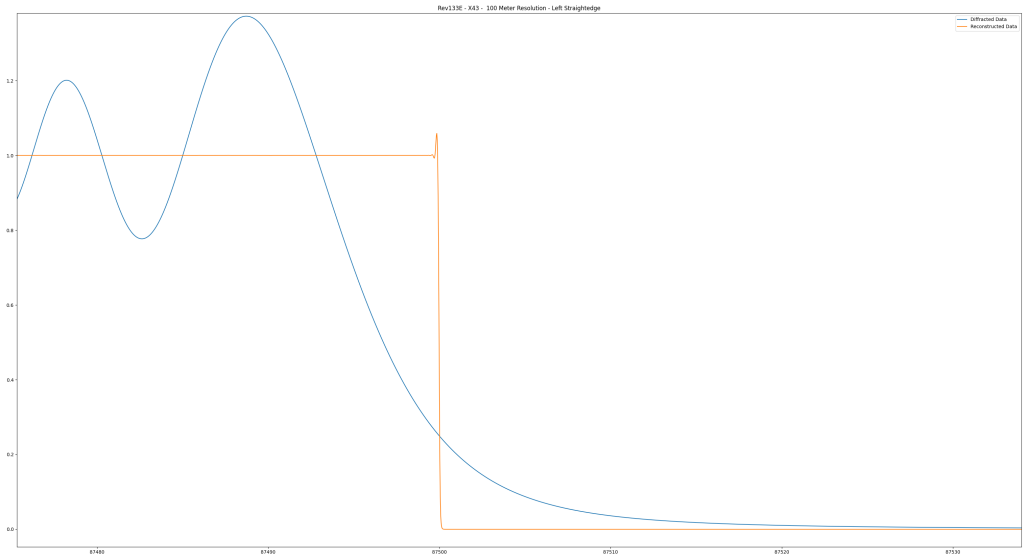

Figure 4. Forward and inverse model for ideal left straightedge at 100 m resolution on Rev133E X43.

The forward model takes the ideal straightedge as input data and applies the perfect ideal Fresnel forward transform given in Eq. (21) to produce the diffracted data $\hat{T}$ (shown as the blue curve in Figure 4). The inverse model then takes in the generated, diffraction-limited $\hat{T}$ as input, and tries to reproduce T via the inverse transform given in Eq. (22). The resulting reconstructed profile is shown as the orange curve.

Even at resolutions as high as 100 m, the new forward and inverse transforms validate the accuracy of the reconstruction. The reconstructed data accurately retrieves the input data, with only a slight overshoot at the top of the straightedge at 87500 km, and identical elsewhere. Notably, this agreement is achieved under the extreme geometry of the Rev133 egress occultation, with a ring opening angle of $B = 1.886°$, providing a stringent test of the model. Such consistency confirms the fine-scale structure seen in our high resolution reconstructions in Section 6 is real.

6. HIGHEST RESOLUTION RECONSTRUCTIONS

We utilize our new Newton reconstruction method to produce opacity profiles at multiple processing resolutions, increased from the 1 km profiles archived on the PDS to the highest resolution of ~ 55 m. In particular, we analyze five morphologically unique structures within the C ring: the Maxwell ringlet, the Titan -1:0 nodal bending wave, a pair of subtle bending waves, and the short wavelength C ring ripples.

6.1. *Maxwell Ringlet*

The first observation is plotted in Figure 5, displaying the reconstructed profile of the Maxwell ringlet for the Rev007E X43 observation, at resolutions ranging from 1 km to 55 m. This density wave structure, believed to be generated by internal oscillations within Saturn itself, provides valuable insights into the forces shaping the rings and how these waves propagate and interact within such a system. Through our reconstructed profiles, we gain information about the fine details and structure of this internally produced wave embedded in a ringlet, revealing resonances tied to Saturn's interior.

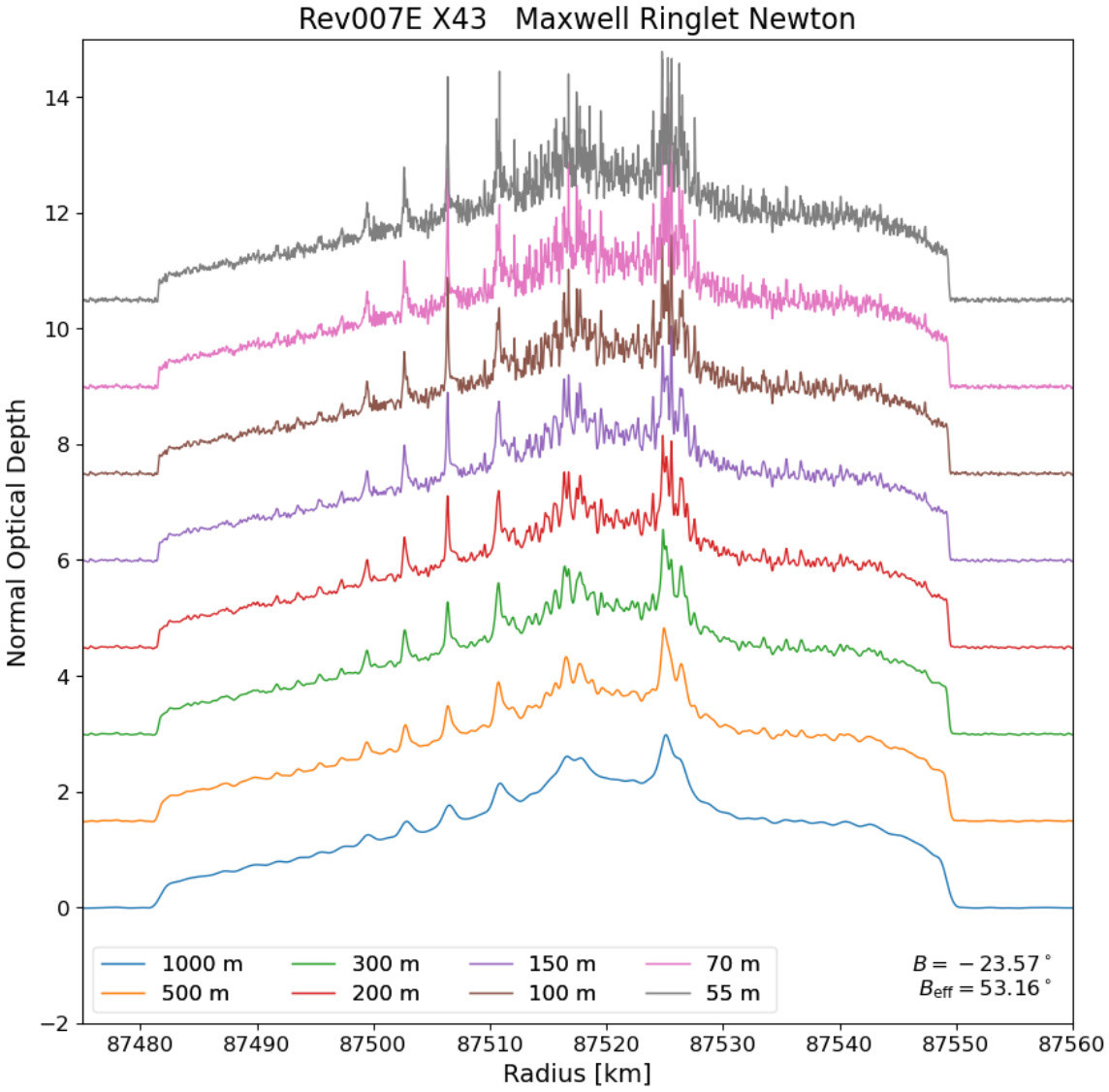

Figure 5. Reconstructed profiles of the Maxwell Ringlet on Rev007E X43 at resolutions from 1 km to 55 m

At 1 km and 500 m resolutions, the ringlet is a broad, smooth hump centered near 87520 km bounded by sharp inner and outer edges located at ∼ 87480 km and ∼ 87550 km. In these reconstructions, the wave appears as four smooth crests whose amplitude peaks near ∼ 87520 km.

As the radial resolution increases beyond 200 m, the central hump is revealed to consist of numerous narrow, sharply defined spikes, with their spacing decreasing toward the resonance center. The persistence of nearly vertical boundaries at the ringlet edges, even at 55 m resolution, further suggests that the Maxwell ringlet is sharply confined. At the finest resolutions, some higher-frequency fluctuations become visible, especially in the densest region between 87510 km and 87530 km, consistent with the expected increase in noise with higher optical depths. In addition, the nearly vertical edges at roughly 87480 km and 87550 km in the 55 m profile suggest very steep optical depth gradients at the ringlet boundaries, whereas the 1 km profile suggests a more gradual transition. Taken together, the results indicate a significant improvement in fine-scale structure to the currently available 1 km reconstructions.

6.2. *Titan −1:0 IVR Bending Wave*

Next, we examine the reconstructions of the Titan −1:0 nodal bending wave for the Rev125I X34 observation, shown in Figure 6.

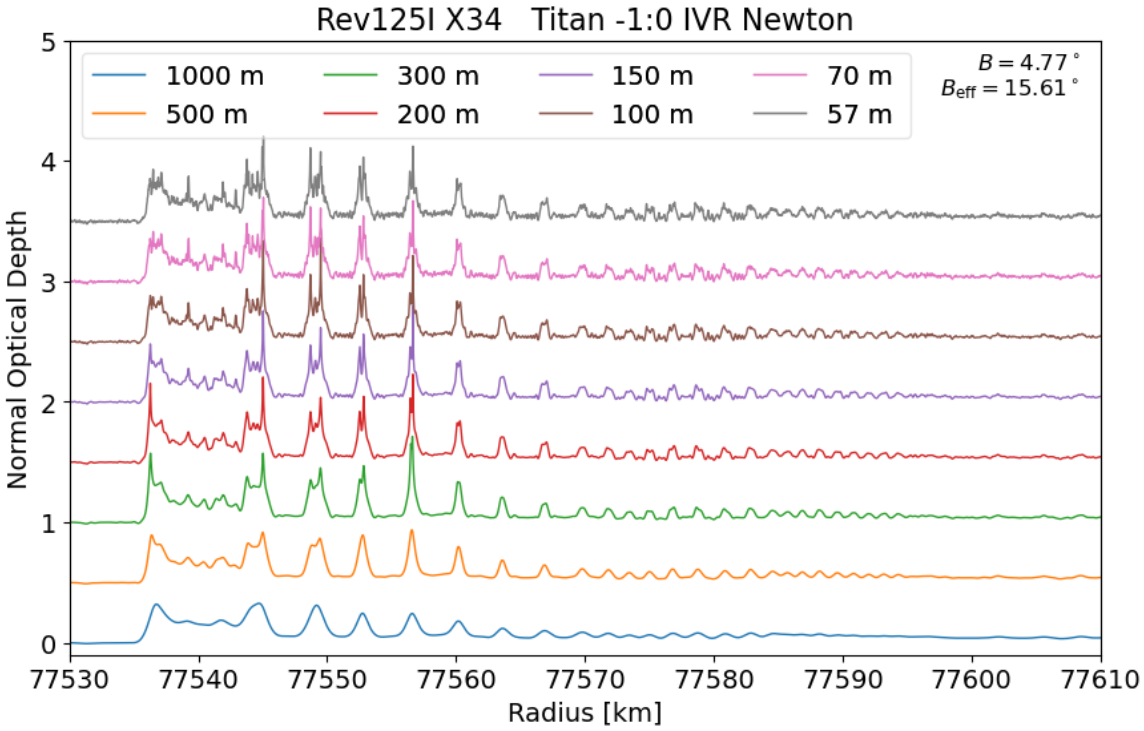

Figure 6. Reconstructed profiles of the Titan −1:0 bending wave on Rev125I X34, at resolutions ranging from 1 km to 57 m

Similar to the Maxwell Ringlet, progressively finer reconstructions transform the apparent structure of the Titan −1:0 bending wave's optical depth profile from smooth undulations into sharply defined peaks. At 1 km resolution, peaks are smooth and blended. Though visible, wave features are indistinct. By 500 to 300 m resolution, the same features begin to show more detail, with the contrast of vertical height between adjacent peaks increasing. Reaching the highest resolutions, several peaks that were previously single become doublets or triplets.

Notably, the radial positions of major peaks remain the same across all reconstructions, indicating that the higher-resolution products are adding spatial detail rather than shifting the underlying signal. To better qualitatively assess

the benefits of high resolution reconstructions, we zoom into the inner region of the Titan −1:0 bending wave, around a radial location of ∼ 77530–77565 km, as shown in Figure 7.

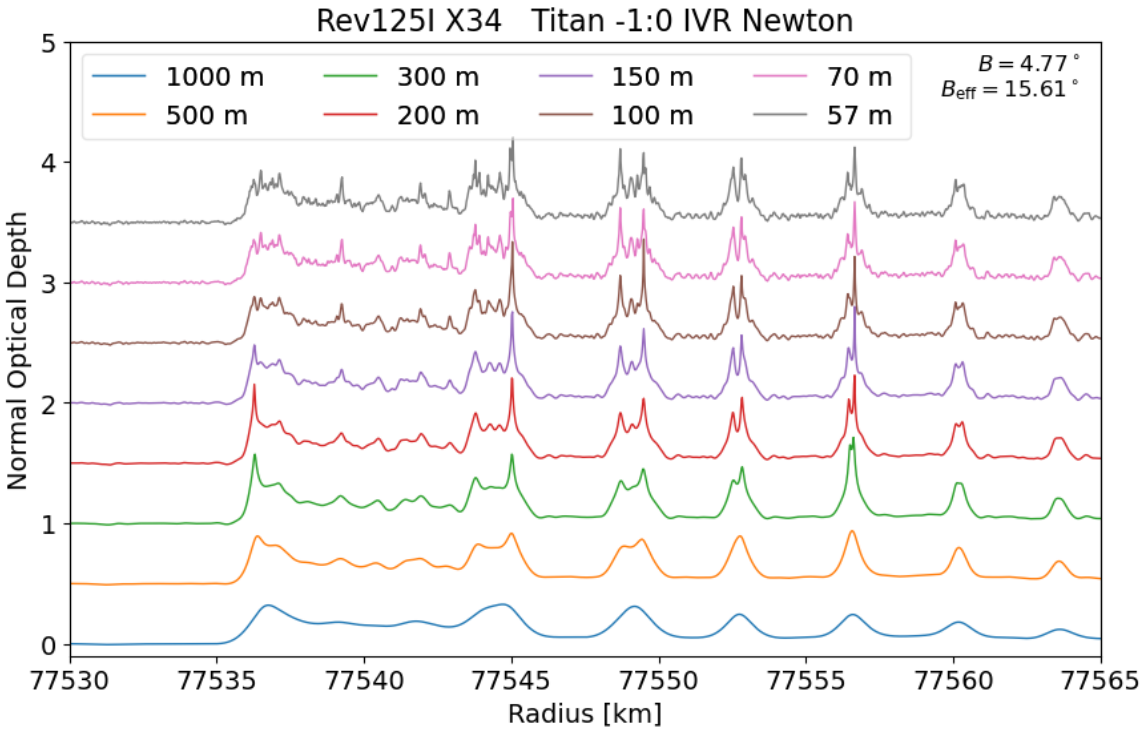

Figure 7. Reconstructed profiles of the inner region of the Titan −1:0 bending wave on Rev125I X34, at resolutions ranging from 1 km to 57 m

The highest resolution reconstructions above of the Titan bending wave are highly significant and reveal a unique advantage: we can now model in detail the vertical extent of the bending wave by looking for signatures of multiple passages through wave crests, something infeasible with only 1 km profiles. The doublet and triplet cusps only seen at higher resolutions in the optical depth profile convey information about the number of line-of-sight crossings of the occultation ray through successive crests. This in turn will provide information about wave damping processes within the ring, an important indicator of how ring particles interact in a disturbed ring.

6.3. *W74.93 (OVR) and W74.94 (OVR)*

We continue by analyzing the reconstructed profile of two vertical bending waves in close proximity, namely W74.93 and W74.94, also examined in French et al. (2019). Figure 8 shows the reconstructed profiles for the two waves for the Rev125I X34 observation. At 1 km resolution, both waves are completely invisible, showing no structure and hints of existing wave features. At 500 m resolution, only a singular subtle bump appears slightly outwards of the resonance location of each wave, but is likewise nearly invisible. As resolution is pushed higher from 300 m to 150 m, the bending waves start to take shape with low-amplitude undulations. When we reach sub-hundred meter resolutions, the smooth undulations become a cluster of sharper peaks, most prominently in W74.94. These results show that a single occultation can yield high-SNR, high-resolution reconstructions of subtle wave features beyond the prominent cases like the Maxwell Ringlet and Titan −1:0 IVR we demonstrated previously, and indicate the potential for high resolution radio reconstructions to clarify unclear wave features.

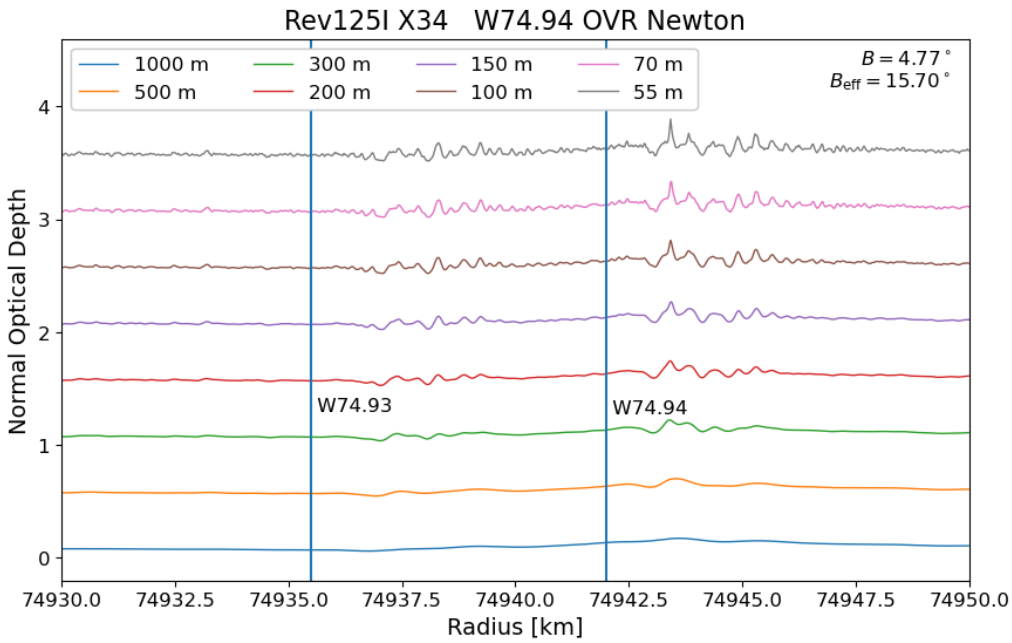

Figure 8. Reconstructed profiles of W74.93 and W74.94 on Rev125I X34 at resolutions ranging from 1 km to 55 m

6.4. *C Ring Ripples*

The C ring ripples are the final feature for which we present high-resolution reconstructions. These short-wavelength, low-amplitude vertical corrugations in Saturn's inner C ring are distinguished by a characteristic "beating" pattern, interpreted as the interference of multiple vertical modes with closely spaced frequencies. We include two reconstructions, one using the Fresnel approximation inversion method (Figure 9), and the other using the Newton inversion method (Figure 10), both using the Rev133I X25 observation.

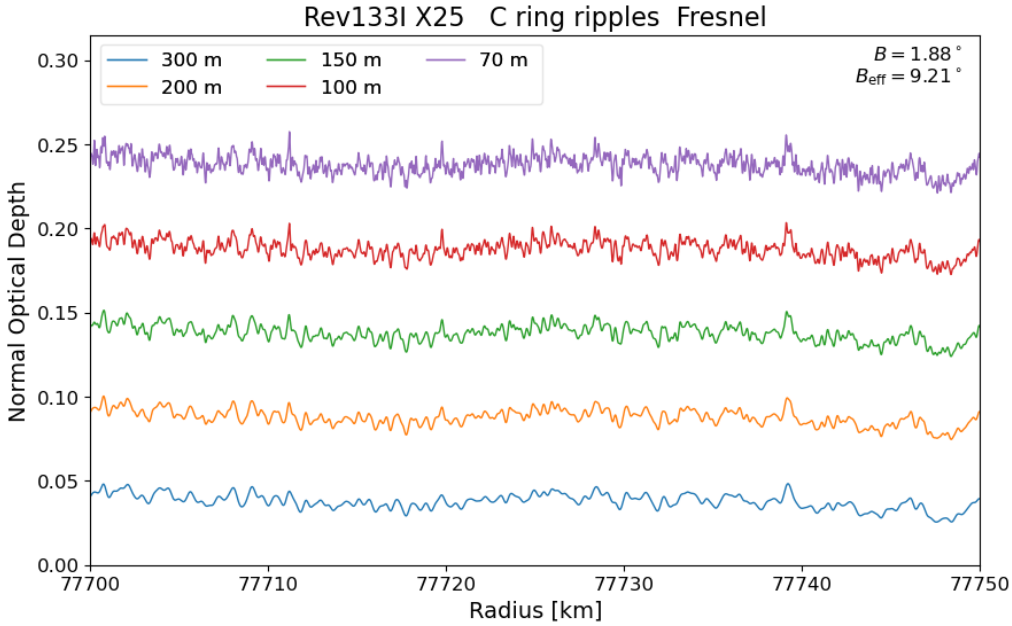

Figure 9. Reconstructed profiles of C ring ripples on Rev133I X25 from the Fresnel method at resolutions ranging from 300 m to 70 m

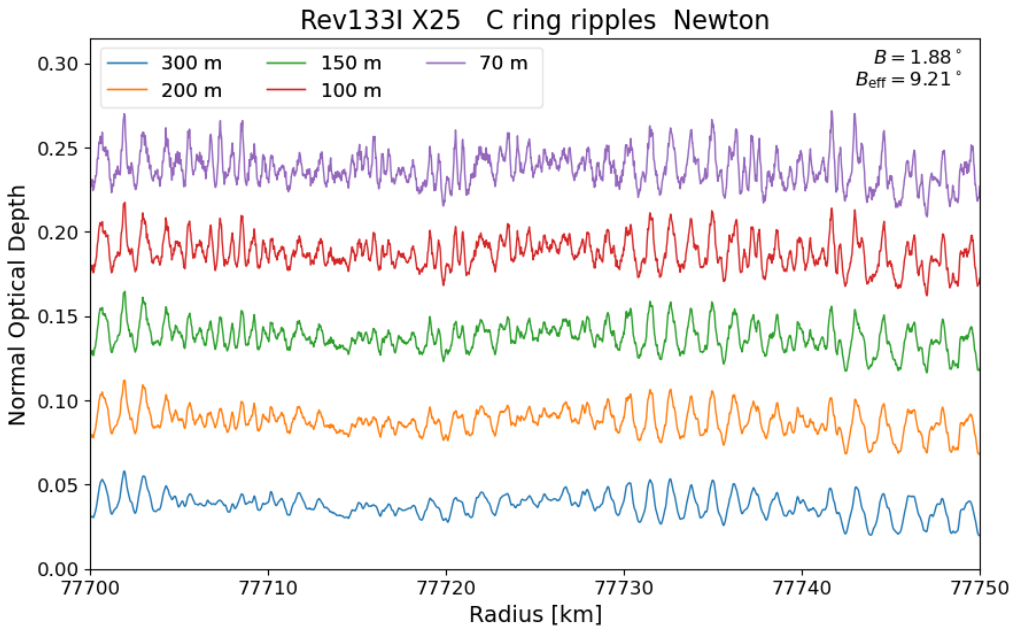

Figure 10. Reconstructed profiles of C ring ripples on Rev133I X25 from the Newton method at resolutions ranging from 300 m to 70 m

Because of their subtle amplitude and sub-kilometer scale, the ripples represent a stringent test for a reconstruction method, particularly under the extreme geometry of Rev133I X25. Resolving this structure requires a high signal-to-noise ratio making the ripples an ideal benchmark. The Fresnel quadratic approximation produces featureless and noisy profiles at all resolutions, failing to reveal either the short-wavelength oscillations or the characteristic beating pattern expected from the superposition of vertical modes. In contrast, the Newton-based reconstruction (Figure 10) recovers clear periodic modulations and reproduces the anticipated beating pattern across all examined resolutions, from 300 m to 70 m. Notably, this fine-scale structure is resolved despite the extremely small amplitude of the signal, with normal optical depth variations below 0.05 throughout the region.

7. DISCUSSION AND CONCLUSION

In this paper, we introduce and validate a novel diffraction inversion technique capable of reconstructing Saturn's ring transmittance profiles from Cassini RSS radio occultations at radial resolutions down to 55 m. Our primary advance is a high-resolution reconstruction technique that, rather than relying on standard polynomial approximations, retains the full Fresnel phase ψ of the diffraction integral and computes the stationary azimuthal angle ϕ_s using the Newton-Raphson method, forgoing many geometric assumptions in the process. To accurately compute the integral over the radius, involving the often highly oscillatory Fresnel kernel, we also incorporate a modification of the Filon quadrature method, accurately integrating real data numerically.

In addition to this Newton-Raphson method, we develop two simpler variants, namely octic and hexadecic Lagrange interpolations of the Fresnel phase, which strike a balance between accuracy and computational efficiency. These variants yield profiles nearly indistinguishable from the Newton approach under the most extreme occultation geometries at resolutions approaching 100 m, still representing nearly an order-of-magnitude improvement over the current best available 1 km optical depth profiles archived in the NASA PDS.

Applying these techniques to the Maxwell ringlet, the Titan −1:0 bending wave, a pair of subtle OVR features (W74.93 and W74.94), and short wavelength C ring ripples, demonstrates the breadth of phenomena that can be newly accessed at high resolution. These applications reveal how previously unresolved fine-scale features become accessible, accentuating the underlying structure of subtle or ambiguous wave signals.

One of the most significant scientific benefits of our high-resolution approach is the newfound ability to directly probe the vertical extent and fine structure of bending waves. For example, sub-100 m reconstructions resolve multiple line-of-sight crossings within a single bending wave, offering constraints on the wave's vertical extent, information unique to RSS among all three of Cassini's occultation instruments (VIMS, UVIS, RSS) and unattainable at kilometer-scale resolution. These advances motivate future investigations involving the analysis of of multiple occultation profiles of a single bending leveraging the differing geometries to construct three-dimensional models of bending wave structure and to probe vertical damping processes across Saturn's rings.

Several predicted outer vertical resonance (OVR) locations in the C ring currently remain devoid of any detectable wave signatures (French et al. 2021). Previous work using VIMS data has demonstrated that phase-corrected wavelet techniques, which co-add multiple stellar occultation profiles, can reveal even extremely subtle wave signatures that are undetectable in individual profiles (French et al. 2021). With our progress in high-resolution radio occultation reconstructions, there is now an opportunity to further enhance the sensitivity of such searches. By integrating these approaches, future studies may be able to systematically survey predicted resonance locations and uncover new, previously hidden waves.

Ultimately, our advances in diffraction reconstruction bring us closer to realizing the full scientific utility of the Cassini RSS dataset, propelling the field of Kronoseimology, and the overall understanding of Saturn's rings.

8. ACKNOWLEDGEMENTS

We are grateful to our mentors, Dr. Richard French and Dr. Ryan Maguire, for their invaluable technical guidance and support throughout our project. We also thank the PRIMES-USA program for providing us with this unique research opportunity.

APPENDIX

A. DERIVATION OF COEFFICIENTS FOR HIGHER-ORDER POLYNOMIAL FITS FOR ψ

We extend the fourth degree Lagrange interpolated polynomial for ψ_F in Marouf et al. (1986) to degree eight. Appendix A of Marouf et al. (1986) provides a fourth order polynomial approximation by matching ψ_F to ψ at four points symmetric about the desired radius ρ, namely, the two midpoints $\rho \pm W/4$ and the two endpoints $\rho \pm W/2$. For our eighth degree approximation, we select eight equidistant points symmetric about ρ, spanning from $\rho - \frac{W}{2}$ to $\rho + \frac{W}{2}$, given by

$$\rho \pm \frac{W}{2}, \rho \pm \frac{3W}{8}, \rho \pm \frac{W}{4}, \rho \pm \frac{W}{8}. \tag{A1}$$

We wish to determine the coefficients $C_1, \ldots, C_8$ for which

$$\psi_F = \sum_{n=1}^{8} C_n (\rho - \rho_0)^n \tag{A2}$$

holds. For each $a \in \{W/2, 3W/8, W/4, W/8\}$, denote

$$\overline{\psi}(a) = \frac{1}{2}[\psi(a) + \psi(-a)], \tag{A3}$$

$$\Delta\psi(a) = \psi(a) - \psi(-a). \tag{A4}$$

For brevity, we write $\overline{\psi}_1 = \overline{\psi}(W/2)$, $\Delta\psi_1 = \Delta\psi(W/2)$, and similarly denote $\overline{\psi}_2$, $\Delta\psi_2$, $\overline{\psi}_3$, $\Delta\psi_3$, $\overline{\psi}_4$, $\Delta\psi_4$, for $\overline{\psi}(3W/8)$, $\Delta\psi(3W/8)$, $\overline{\psi}(W/4)$, $\Delta\psi(W/4)$, $\overline{\psi}(W/8)$, $\Delta\psi(W/8)$, respectively. Substituting values into the ψ_F, we obtain the equations

$$C_1\left(\frac{W}{2}\right) + C_3\left(\frac{W}{2}\right)^3 + C_5\left(\frac{W}{2}\right)^5 + C_7\left(\frac{W}{2}\right)^7 = \frac{\Delta\psi_1}{2}, \tag{A5}$$

$$C_1\left(\frac{3W}{8}\right) + C_3\left(\frac{3W}{8}\right)^3 + C_5\left(\frac{3W}{8}\right)^5 + C_7\left(\frac{3W}{8}\right)^7 = \frac{\Delta\psi_2}{2}, \tag{A6}$$

$$C_1\left(\frac{W}{4}\right) + C_3\left(\frac{W}{4}\right)^3 + C_5\left(\frac{W}{4}\right)^5 + C_7\left(\frac{W}{4}\right)^7 = \frac{\Delta\psi_3}{2}, \tag{A7}$$

$$C_1\left(\frac{W}{8}\right) + C_3\left(\frac{W}{8}\right)^3 + C_5\left(\frac{W}{8}\right)^5 + C_7\left(\frac{W}{8}\right)^7 = \frac{\Delta\psi_4}{2} \tag{A8}$$

for terms of odd order, and

$$C_2\left(\frac{W}{2}\right)^2 + C_4\left(\frac{W}{2}\right)^4 + C_6\left(\frac{W}{2}\right)^6 + C_8\left(\frac{W}{2}\right)^8 = \overline{\psi}_1, \tag{A9}$$

$$C_2\left(\frac{3W}{8}\right)^2 + C_4\left(\frac{3W}{8}\right)^4 + C_6\left(\frac{3W}{8}\right)^6 + C_8\left(\frac{3W}{8}\right)^8 = \overline{\psi}_2, \tag{A10}$$

$$C_2\left(\frac{W}{4}\right)^2 + C_4\left(\frac{W}{4}\right)^4 + C_6\left(\frac{W}{4}\right)^6 + C_8\left(\frac{W}{4}\right)^8 = \overline{\psi}_3, \tag{A11}$$

$$C_2\left(\frac{W}{8}\right)^2 + C_4\left(\frac{W}{8}\right)^4 + C_6\left(\frac{W}{8}\right)^6 + C_8\left(\frac{W}{8}\right)^8 = \overline{\psi}_4 \tag{A12}$$

for terms of even order. Solving both systems, we obtain the coefficients

$$C_1 = \frac{672\Delta\psi_1 - 168\Delta\psi_2 + 32\Delta\psi_3 - 3\Delta\psi_4}{105W}, \tag{A13}$$

$$C_2 = \frac{4\left(8064\overline{\psi}_1 - 1008\overline{\psi}_2 + 128\overline{\psi}_3 - 9\overline{\psi}_4\right)}{315W^2}, \tag{A14}$$

$$C_3 = \frac{16\left(-488\Delta\psi_1 + 338\Delta\psi_2 - 72\Delta\psi_3 + 7\Delta\psi_4\right)}{45W^3}, \tag{A15}$$

$$C_4 = \frac{64\left(-1952\overline{\psi}_1 + 676\overline{\psi}_2 - 96\overline{\psi}_3 + 7\overline{\psi}_4\right)}{45W^4}, \tag{A16}$$

$$C_5 = \frac{2048\left(29\Delta\psi_1 - 26\Delta\psi_2 + 9\Delta\psi_3 - \Delta\psi_4\right)}{45W^5}, \tag{A17}$$

$$C_6 = \frac{8192\left(116\overline{\psi}_1 - 52\overline{\psi}_2 + 12\overline{\psi}_3 - \overline{\psi}_4\right)}{45W^6}, \tag{A18}$$

$$C_7 = \frac{65536\left(-14\Delta\psi_1 + 14\Delta\psi_2 - 6\Delta\psi_3 + \Delta\psi_4\right)}{315W^7}, \tag{A19}$$

$$C_8 = \frac{262144\left(-56\overline{\psi}_1 + 28\overline{\psi}_2 - 8\overline{\psi}_3 + \overline{\psi}_4\right)}{315W^8}, \tag{A20}$$

used in the octic Lagrange interpolation of ψ. The coefficients for the 16^{th} degree interpolating polynomial are calculated in a similar fashion.

B. SIMPLIFYING INTEGRAL WITH STATIONARY PHASE APPROXMATION

We provide the full derivation for collapsing the double integral

$$\hat{T}(\rho_0) = \frac{\mu_0}{i\lambda}\int_0^\infty \rho T(\rho)\int_0^{2\pi}\frac{\exp(i\psi(\boldsymbol{\rho},\boldsymbol{\rho}_0,\mathbf{R}))}{\|\mathbf{R}-\boldsymbol{\rho}\|}d\phi d\rho \tag{B1}$$

to

$$\hat{T}(\rho_0) \approx \frac{1-i}{2F}\int_0^\infty T(\rho)\exp(i\psi(\boldsymbol{\rho}_s,\boldsymbol{\rho}_0,\mathbf{R}))d\rho, \tag{B2}$$

going from Eq. (20) to Eq. (21). We apply the stationary phase approximation on the ϕ integral about some critical point $\phi=\phi_s$, the solution to $\partial\psi/\partial\phi=0$. It follows

$$\int_0^{2\pi}\frac{\exp(i\psi(\boldsymbol{\rho},\boldsymbol{\rho}_0,\mathbf{R}))}{\|\mathbf{R}-\boldsymbol{\rho}\|}d\phi \approx \int_{\phi_s-\varepsilon}^{\phi_s+\varepsilon}\frac{\exp(i\psi(\boldsymbol{\rho}_s,\boldsymbol{\rho}_0,\mathbf{R}))}{\|\mathbf{R}-\boldsymbol{\rho}_s\|}d\phi \tag{B3}$$

$$\approx \int_{\phi_s-\varepsilon}^{\phi_s+\varepsilon}\frac{\exp\left(i(\psi(\boldsymbol{\rho}_s,\boldsymbol{\rho}_0,\mathbf{R})+\frac{1}{2}\psi''(\boldsymbol{\rho}_s,\boldsymbol{\rho}_0,\mathbf{R})(\phi-\phi_s)^2\right)}{\|\mathbf{R}-\boldsymbol{\rho}_s\|}d\phi. \tag{B4}$$

Applying a change of variables $u=\sqrt{\frac{\psi''}{2}}(\phi-\phi_s)^2$, the integral further reduces to

$$\frac{\exp(i\psi(\boldsymbol{\rho}_s,\boldsymbol{\rho}_0,\mathbf{R}))}{\|\mathbf{R}-\boldsymbol{\rho}_s\|}\sqrt{\frac{2}{\psi''}}\int_{-\infty}^{\infty}\exp(iu^2)du = \frac{\exp(i\psi(\boldsymbol{\rho}_s,\boldsymbol{\rho}_0,\mathbf{R}))}{\|\mathbf{R}-\boldsymbol{\rho}_s\|}\sqrt{\frac{2}{\psi''}}\int_{-\infty}^{\infty}\cos(u^2)+i\sin(u^2)du \tag{B5}$$

$$= \frac{\exp(i\psi(\boldsymbol{\rho}_s,\boldsymbol{\rho}_0,\mathbf{R}))}{\|\mathbf{R}-\boldsymbol{\rho}_s\|}\sqrt{\frac{2}{\psi''}}\left(2\int_0^{\infty}\cos(u^2)+i\sin(u^2)du\right) \tag{B6}$$

$$= \frac{\exp(i\psi(\boldsymbol{\rho}_s,\boldsymbol{\rho}_0,\mathbf{R}))}{\|\mathbf{R}-\boldsymbol{\rho}_s\|}\sqrt{\frac{\pi}{\psi''}}(1+i). \tag{B7}$$

Substituting this expression back into the original double integral, we obtain

$$\frac{\mu_0}{i\lambda}\int_0^\infty \rho T(\rho)\frac{\exp(i\psi(\boldsymbol{\rho}_s,\boldsymbol{\rho}_0,\mathbf{R}))}{\|\mathbf{R}-\boldsymbol{\rho}_s\|}\sqrt{\frac{\pi}{\psi''}}(1+i)d\rho = \frac{(1-i)\sin B}{\lambda}\int_0^\infty \rho T(\rho)\frac{\exp(i\psi(\boldsymbol{\rho}_s,\boldsymbol{\rho}_0,\mathbf{R}))}{\|\mathbf{R}-\boldsymbol{\rho}_s\|}\sqrt{\frac{\pi}{\psi''}}d\rho. \tag{B8}$$

Writing ψ'' as it comes from the Rayleigh-Sommerfeld equation

$$\psi''(\boldsymbol{\rho}_s,\boldsymbol{\rho}_0,\mathbf{R}) = \frac{F^2\sin^2(B)4\pi\rho^2}{\lambda^2\|\mathbf{R}-\boldsymbol{\rho}_s\|^2}, \tag{B9}$$

Eq. (B8) becomes

$$\frac{(1-i)\sin B}{\lambda}\int_0^\infty \rho T(\rho)\frac{\exp(i\psi(\boldsymbol{\rho}_s,\boldsymbol{\rho}_0,\mathbf{R}))}{\|\mathbf{R}-\boldsymbol{\rho}_s\|}\sqrt{\frac{\lambda^2\|\mathbf{R}-\boldsymbol{\rho}_s\|^2}{4F^2\sin^2 B\rho^2}}d\rho = \frac{1-i}{2F}\int_0^\infty T(\rho)\exp(i\psi(\boldsymbol{\rho}_s,\boldsymbol{\rho}_0,\mathbf{R}))d\rho, \tag{B10}$$

completing the derivation.

REFERENCES

Afigbo, V. M. and 6 colleagues 2025. Unveiling What Makes Saturn Ring: Quantifying the Amplitudes of Saturn's Planetary Normal-Mode Oscillations and Trends in C Ring Properties Using Kronoseismology (VII). Journal of Geophysical Research (Planets) 130. doi:10.1029/2024JE008710

Born, M., Wolf, E. 2019. Principles of Optics. Principles of Optics, by Max Born, Emil Wolf, Print 2019, ebook 2020. Cambridge: Cambridge University Press. eISBN: 9781108769914.. doi:10.1017/9781108769914

Colwell, J. E., Nicholson, P. D., Tiscareno, M. S., et al. 2009, Saturn from Cassini-Huygens, The Structure of Saturn's Rings, 375. doi:10.1007/978-1-4020-9217-6_13

Colwell, J. E., Esposito, L. W., Jerousek, R. G., Sremčević, M., Pettis, D., Bradley, E. T. 2010. Cassini UVIS Stellar Occultation Observations of Saturn's Rings. The Astronomical Journal 140, 1569–1578. doi:10.1088/0004-6256/140/6/1569

French, R. G., McGhee-French, C. A., Nicholson, P. D., et al. 2019, Icarus, Kronoseismology III: Waves in Saturn's inner C ring, 319, 599. doi:10.1016/j.icarus.2018.10.013

French, R. G., Bridges, B., Hedman, M. M., et al. 2021, Icarus, Kronoseismology V: A panoply of waves in Saturn's C ring driven by high-order internal planetary oscillations, 370, 114660. doi:10.1016/j.icarus.2021.114660

French, R. G., Nicholson, P. D., Hedman, M. M., et al. 2025, Icarus, Further reverberations of the 1983 impact with Saturn's C ring, 431, 116463. doi:10.1016/j.icarus.2025.116463

Gresh, D. L., Marouf, E. A., Tyler, G. L., Rosen, P. A., Simpson, R. A. 1989. Voyager radio occultation by Uranus' rings I. Observational results. Icarus, 78, 131–168. doi:10.1016/0019-1035(89)90074-2

Hedman, M. M. and 10 colleagues 2007. Saturn's dynamic D ring. Icarus 188, 89–107. doi:10.1016/j.icarus.2006.11.017

Hedman, M. M., Burns, J. A., Evans, M. W., Tiscareno, M. S., Porco, C. C. 2011. Saturn's Curiously Corrugated C Ring. Science 332, 708. doi:10.1126/science.1202238

Hedman, M. M., & Nicholson, P. D. 2013. Kronoseismology: Using Density Waves in Saturn's C Ring to Probe the Planet's Interior. AJ, 146, 12. doi:10.1088/0004-6256/146/1/12

Hedman, M. M., Nicholson, P. D. 2014. More Kronoseismology with Saturn's rings. Monthly Notices of the Royal Astronomical Society 444, 1369–1388. doi:10.1093/mnras/stu1503

Hedman, M. M., Nicholson, P. D., French, R. G. 2019. Kronoseismology. IV. Six Previously Unidentified Waves in Saturn's Middle C Ring. The Astronomical Journal 157. doi:10.3847/1538-3881/aaf0a6

Hedman, M. M., Nicholson, P. D., El Moutamid, M., et al. 2022, PSJ, Kronoseismology. VI. Reading the Recent History of Saturn's Gravity Field in Its Rings, 3, 3, 61. doi:10.3847/PSJ/ac4df8

Kliore, A. J. and 12 colleagues 2004. Cassini Radio Science. Space Science Reviews 115, 1–70. doi:10.1007/s11214-004-1436-y

Marley, M. S. & Porco, C. C. 1993, Icarus, Planetary Acoustic Mode Seismology: Saturn's Rings, 106, 2, 508. doi:10.1006/icar.1993.1189

Marouf, E. A., Tyler, G. L., Eshleman, V. R. 1982. Theory of radio occultation by Saturn's rings. Icarus 49, 161–193. doi:10.1016/0019-1035(82)90070-7

Marouf, E. A., Tyler, G. L., Rosen, P. A. 1986. Profiling Saturn's rings by radio occultation. Icarus, 68, 120–166. doi:10.1016/0019-1035(86)90078-3

Mankovich, C. R. & Fuller, J. 2021, Nature Astronomy, A diffuse core in Saturn revealed by ring seismology, 5, 1103. doi:10.1038/s41550-021-01448-3

NASA/JPL-Caltech/Space Science Institute. 2008, PIA10501: Two Kinds of Wave, https://photojournal.jpl.nasa.gov/catalog/PIA10501

NASA/JPL-Caltech/Space Science Institute. 2017a, PIA21627: Staggering Structure, https://photojournal.jpl.nasa.gov/catalog/PIA21627

NASA/JPL-Caltech/Space Science Institute. 2017b, PIA21056: Daphnis Up Close, https://photojournal.jpl.nasa.gov/catalog/PIA21056

NASA/JPL-Caltech/Space Science Institute. 2018, PIA22418: Gravity's Rainbow, https://photojournal.jpl.nasa.gov/catalog/PIA22418

Nicholson, P. D. and 11 colleagues 2020. Occultation observations of Saturn's rings with Cassini VIMS. Icarus 344. doi:10.1016/j.icarus.2019.06.017

Nicholson, P., French, R., Hedman, M., et al. 2025, AAS/Division of Dynamical Astronomy Meeting, Ripples in the C ring: echoes of the 1983 impact?, 57, 3, 303.05.

PDS Rings Node. 2025. Planetary Data System: Rings Node. NASA Planetary Data System. https://pds-rings.seti.org/

Porco, C. C. and 34 colleagues 2005. Cassini Imaging Science: Initial Results on Saturn's Rings and Small Satellites. Science 307, 1226–1236. doi:10.1126/science.1108056

Shu, F. H. 1984, IAU Colloq. 75: Planetary Rings, Waves in planetary rings, 513.